

METCRAX 2006

Meteorological Experiments in Arizona's Meteor Crater

BY C. DAVID WHITEMAN, ANDREAS MUSCHINSKI, SHARON ZHONG, DAVID FRITTS, SEBASTIAN W. HOCH, MAURA HAHNENBERGER, WENQING YAO, VINCENT HOHREITER, MARIO BEHN, YONGHUN CHEON, CRAIG B. CLEMENTS, THOMAS W. HORST, WILLIAM O. J. BROWN, AND STEVEN P. ONCLEY

Field and numerical studies of the evolution of the atmosphere in the near-ideal, basin-shaped crater have led to an extensive dataset exhibiting many stable boundary layer phenomena and their interactions with background flows.

A month-long meteorological field experiment called the Meteor Crater Experiment (METCRAX 2006) was conducted in October 2006 in Meteor Crater, near Winslow, Arizona. METCRAX focused on two research topics. First, the

meso- and microscale structure and evolution of the stable boundary layer in and around the crater were studied to gain a better understanding of the physical processes that govern the evolution of cold-air pools. This research should be relevant for a wide range of applied and theoretical problems dealing with the meteorology of stable boundary layers. A second objective was to determine whether an analog to lake and ocean seiches (i.e., standing waves in hydrologic basins) occurs in the crater atmosphere and what role basin-scale seiches and internal wave motions play in transport and mixing in basin stable layers. This research is thought to be the first in-depth observational and computational study of standing waves in atmospheric basins.

A number of research questions guided the planning of this experiment and governed the choices of field instrumentation and operating procedures. Selected research questions relevant to the stated objectives are given in Tables 1 and 2.

The field observations were designed to capture 1) the diurnal cycle of buildup and breakup of the cold-air pool, 2) the characteristics of seiches and other wave motions in the crater atmosphere, 3) the mean and turbulence characteristics of slope flows

AFFILIATIONS: WHITEMAN, HOCH, AND HAHNENBERGER—University of Utah, Salt Lake City, Utah; MUSCHINSKI, HOHREITER, BEHN, AND CHEON—University of Massachusetts at Amherst, Amherst, Massachusetts; ZHONG AND YAO—Michigan State University, East Lansing, Michigan; FRITTS—Colorado Research Associates, Division of NorthWest Research Associates, Boulder, Colorado; CLEMENTS—San Jose State University, San Jose, California; HORST, BROWN, AND ONCLEY—National Center for Atmospheric Research, Boulder, Colorado

CORRESPONDING AUTHOR: C. David Whiteman, Meteorology Department, University of Utah, 135 S 1460 E, Rm 819, Salt Lake City, UT 84112-0110
E-mail: dave.whiteman@utah.edu

The abstract for this article can be found in this issue, following the table of contents.

DOI:10.1175/2008BAMS2574.1

In final form 7 May 2008
©2008 American Meteorological Society

TABLE 1. Selected research questions: Cold air pools.

Cold air pools
<ul style="list-style-type: none"> • What are the key terms in the mass, momentum, heat and moisture budgets of the basin atmosphere during a diurnal cycle? How do these compare to budgets over valleys and plains?
<ul style="list-style-type: none"> • What roles do up- and downslope flows on the sidewalls play in the buildup and breakup of basin inversions? How do the roles vary as the characteristics of slope flows change with evolving ambient stability within the basin?
<ul style="list-style-type: none"> • What effect does asymmetry of solar heating within the basin have on the breakup of the inversion? How does this asymmetry affect the growth of boundary layers, the horizontal homogeneity of the stable core, and the horizontal variation of subsidence (which compensates for upslope flows on the sidewalls) across the basin?
<ul style="list-style-type: none"> • How are basin cooling and potential temperature structure affected by ambient flows above the basin and by surface radiation and energy budget factors (including dewfall) inside the basin? What roles do radiative flux divergence, soil heat flux, and infrared back-radiation from the sidewalls play in the nocturnal cooling of the basin atmosphere?

on the crater sidewalls, 4) the radiative fluxes and other surface energy budget components at the crater surface and in its atmosphere, and (5) the influence of ambient winds and stratification on the crater meteorology. The observations span length scales from centimeters to tens of kilometers and time scales from tens of milliseconds to weeks.

The METCRAX program is a 3-yr collaborative research program involving students and four principal investigators (the first four coauthors of this paper) from several institutions. The data from the field program are supporting basic meteorological analyses as well as simulations with mesoscale, large-eddy simulation, and direct numerical simulation models to gain an improved understanding of boundary layer meteorology in the uncomplicated topography of the crater. This article provides an overview of the METCRAX field program and presents some initial analyses.

PREVIOUS RESEARCH. Meteorological research programs often select experimental sites with topography that allows simplification of the experimental design. Some programs have selected horizontally homogeneous terrain, for example, the Kansas (Haugen et al. 1971) and Wangara experi-

ments (Clarke et al. 1971), or gently dissected terrain [Cooperative Atmosphere–Surface Exchange Study (CASES-99); Poulos et al. 2002]. The uniform slope of Rattlesnake Mountain near Richland, Washington, was selected for investigations of thermally driven downslope flows (Doran and Horst 1983; Horst and Doran 1986). Cinder Cone Butte, a bell-shaped hill on the Snake River Plain, was the site for the study of the impactation of air pollution plumes on isolated hillsides, a problem also studied in laboratory tow tanks (Schiermeier et al. 1983). Recently, the Owens Valley of California was selected for the Terrain-Induced Rotor Experiment (Grubišić et al. 2008) because the unusually steep and uniform “two-dimensional” Sierra Nevada ridgeline upwind of the valley frequently generates lee waves and, occasionally, rotors.

Several exploratory meteorological experiments have been conducted previously in small basins that were not as ideally shaped as Meteor Crater. These include the Sinbad basin of Colorado (Whiteman et al. 1996), the Peter Sinks basin of Utah (Clements et al. 2003), and the Gruenloch basin of Austria (Steinacker et al. 2007). Investigations of mass, momentum, heat, and moisture budgets in these basins, conducted with limited observational resources, pointed out the important role of the surrounding topography and the complicating effects of advection. These results suggested that extensive experiments in more idealized enclosed basins would have significant advantages

TABLE 2. Selected research questions: Seiches.

Seiches
<ul style="list-style-type: none"> • What role do seiches play in transport and mixing in the cold-air pool in a closed basin?
<ul style="list-style-type: none"> • How well can seiches be identified in pressure, temperature, and velocity data?
<ul style="list-style-type: none"> • What modes of seiches are excited in Meteor Crater, and how do their structures depend on forcing and cold pool stability?
<ul style="list-style-type: none"> • What is the altitude dependence of seiche characteristics, and how do they evolve during the night?
<ul style="list-style-type: none"> • To what extent, and in what respect, do simulations agree with observed seiches?
<ul style="list-style-type: none"> • How well do modeled and observed seiches and internal waves agree in their structures and decay rates? How well are the amplitudes of the seiches correlated with the ambient-wind energy contained in specific frequency bands?
<ul style="list-style-type: none"> • What are the decay times of the potential and kinetic energy of the seiches?

for answering extant questions on the physical processes leading to temperature inversion or cold pool buildup and breakup in situations where large-scale advective influences from outside the basin might be reduced or absent.

While we are unaware of any other meteorological investigations of meteorite craters on Earth, there is an ongoing study of Martian craters using meteorological sensors on board remotely piloted Martian “rovers.” The vertical temperature structure of the Martian atmospheric boundary layer to depths of 2 km is presently being studied using upward-looking thermal emission spectrometers from the Spirit and Opportunity rovers on the Martian surface (Smith et al. 2004, 2006) and the Opportunity rover is presently investigating the Victoria Crater, which is similar in size to Meteor Crater. The observations are raising interesting questions about the role of meteorology in surficial geological and geophysical processes in and near Martian craters, including the wind transport of dust.

METEOR CRATER. Meteor Crater, a near-circular crater approximately 40 km east of Flagstaff in northern Arizona, was produced by the impact of a 40- to 50-m-diameter meteorite that struck the Colorado Plateau about 49,000 yr ago (Phillips et al. 1991). Meteor Crater is owned by the Barringer Crater Company, a private foundation in Flagstaff, Arizona, that promotes the use of the crater for scientific and educational purposes. A modern visitor center/museum on the north rim of the crater operated by their leaseholder, Meteor Crater Enterprises, Inc., serves the needs of tourism at this unique natural attraction. The crater itself is closed to the public to preserve its future scientific value for crater impact and geological studies, and scientific experiments

can be conducted in the crater only with permission granted through the Barringer Crater Company’s internal scientific peer-review process. Prior to METCRAX, the scientific usage of the crater was limited to geological and geophysical investigations related to the meteorite impact.

Meteor Crater (see Fig. 1) is the best preserved impact crater on Earth. It is relatively recent in geological terms, and it is in a semiarid area of low precipitation where erosion is minimized. Nevertheless, erosion has incised gullies in the walls of the crater, and the crater floor has, over time, filled with alluvium and windblown dust. At the center of the crater floor is a nearly level *playa* or dry lake bed that is covered with water during wet periods. A semipermanent lake is thought to have formed in the crater during wet intervals of the geological record (D. Kring 2005, personal communication). The crater exposes three distinct rock layers that are visible on the crater sidewalls. From top to bottom these horizontal strata, which differ in appearance, are Moenkopi siltstone, Kaibab limestone, and Coconino sandstone (Wright and Ramsey 2006). Exposed high-angle cliffs are present on the upper crater sidewalls, grading progressively into boulders, talus, scree, and layered soil alluvium as the crater floor is approached. The crater has a sparse cover of grasses and bushes, and subtle differences in vegetation type and coverage occur in different microclimatic zones in the crater associated with solar radiation input, water availability, and seasonal differences in shadowing by the surrounding rim topography.

The crater is approximately 165 m in depth and 1.2 km in diameter at the rim. The crater rim is about 50 m above the level of the surrounding plain of the Colorado Plateau, and the ridge line is unbroken by major saddles or passes (Fig. 2). The crater is, to a



FIG. 1. Panorama of Meteor Crater looking east from Barringer Point, one of the peaks on the west rim. Sebastian Hoch photo.

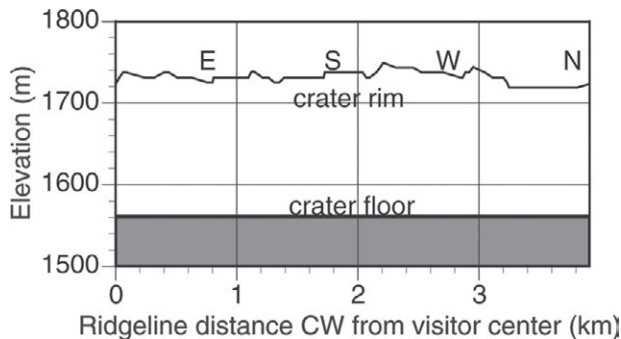


FIG. 2. Ridge crest elevation as a function of distance clockwise around the crater. The mean crest height, h_c , is about 1,733 m MSL.

first approximation, an axisymmetric circular basin, although the somewhat enhanced erosion along two faults that cross the crater floor from northwest to southeast and from southwest to northeast give the crater a slightly squared-off geometry.

The uniform ridge height and symmetrical sidewalls of Meteor Crater make it an appropriate experimental site for studying both cold pools and seiches. Flows within the crater are on a sufficiently small scale to allow the Coriolis force to be neglected in modeling studies, and the crater is sufficiently deep to protect the cold pool from direct effects of large-scale advection when a stable boundary layer is present in the crater. On the other hand, crater-scale fluctuations of the ambient wind (from any direction) induce crater-scale pressure fluctuations, which are expected to trigger seiches in the interior of the cold pool. These seiches, in turn, are expected to generate the small-scale turbulence that governs the diffusivity of heat and humidity and therefore have an effect on the vertical temperature and humidity gradients in the cold pool. Because of the crater's simple geometry and the absence of complex topography in the immediate vicinity of the crater, stable boundary layer structure and evolution can be studied in a laboratory-like setting.

THE METCRAX FIELD EXPERIMENT

DESIGN. The 1–31 October experimental period was chosen to follow the July through mid-September monsoonal period when cloudiness and thunderstorms affect the area. October was expected to provide a suitable mix of fine weather that would favor the development of inversions in the crater and passing synoptic disturbances that could excite seiches in the crater. Field equipment from the National Center for Atmospheric Research (NCAR) was also available during October.

Most of the field instrumentation operated continuously during the 1-month field program. Some additional meteorological equipment, however, was operated during overnight periods when skies were clear and background winds were weak. These intensive observational periods (IOPs; Table 3) investigated the evolution of nocturnal temperature inversions in the crater and their relationship with atmospheric structure outside the crater. The data collected during these periods should also provide enhanced support for postexperiment modeling efforts. IOPs began at 1500 LT and continued until the nocturnal temperature inversion broke up the next morning, usually by 1000 LT. IOP days were selected on the basis of 24-h forecasts, with confirmation on the morning of the IOP. Special IOP observations included synchronous tethered flights from three sites on the crater floor and 3-hourly rawinsonde launches from a site outside the crater.

A third mode of operation supplemented the continuous and IOP observations to obtain additional information on seiches and internal waves. In this mode, high-frequency wind profiles were made using sonic anemometers on masts at two sites on the crater's rim. Additionally, high-frequency temperature profiles were made with temperature data loggers from portable masts that were operated for several days at a given location and then moved to other sites of interest.

SITES AND INSTRUMENTATION. Meteor Crater presented logistical difficulties, as there are no access roads into the crater and no services (power, lighting, communications, water, or sanitary facilities) available there. The meteorological and support equipment was ferried into and out of the crater by helicopter, with technicians and field personnel carrying additional equipment into and out of the crater on a steep hiking trail used in the 1960s by

TABLE 3. Intensive observational periods, October 2006.

IOP No.	Dates
1	7–8 Oct
2	11–12 Oct
3	18–19 Oct
4	20–21 Oct
5	22–23 Oct
6	28–29 Oct
7	30–31 Oct

TABLE 4. ISFF and ISS tower site characteristics. Dashes indicate horizontal surfaces.

Site name	ID	Lat (°W)	Lon (°N)	Altitude (m MSL)	Slope azimuth (° true)	Slope angle (°)
Crater rim	RIM	111.0292	35.0295	1,744	—	—
Crater floor	FLR	111.0225	35.0280	1,563	—	—
West upper	WU	111.0270	35.0274	1,609	88	22
West lower	WL	111.0255	35.0272	1,572	70	4
East upper	EU	111.0184	35.0272	1,600	264	24
East lower	EL	111.0198	35.0272	1,572	266	7
Southwest	SW	111.0388	35.0103	1,697	—	—
ISS	NW	111.0342	35.0722	1,670	—	—

astronauts training in the crater. Access to the crater was strictly limited to field personnel.

Power in the crater was supplied by solar panels coupled to rechargeable storage batteries and by gasoline-powered generators. Communications between tethered teams inside the crater and rawinsonde operators outside the crater were handled by a radio repeater and handheld radios loaned to the experimental teams by Meteor Crater Enterprises. Walkie-talkies were used for communications inside the crater. Water was backpacked in by field personnel and a portable toilet, slung into the crater by helicopter and rather poorly camouflaged, was set up on the crater floor, much to the amusement of the crater museum visitors, who were able to watch activities in the crater through telescopes at the crater visitor center on the north rim.

The bulk of the continuously operating METCRAX meteorological instrumentation was supplied, installed, and operated by NCAR's Earth Observing Laboratory in Boulder, Colorado, through funding from the National Science Foundation (NSF). Additional equipment was supplied and operated by the principal investigators.

The meteorological equipment used in the field experiment fell into the following two categories: 1) equipment to measure the background meteorology above and upwind of the crater, 2) equipment deployed inside the crater. The locations of the major NCAR meteorological instrumentation sites operated both inside and outside the crater are given in Table 4. Detailed information on the meteorological equipment at these sites and real-time field data are provided online (NCAR 2008a,b).

Background meteorology outside the crater. The background atmospheric conditions above the Colorado Plateau were monitored continuously with NCAR's

Integrated Sounding System (ISS), which is described online (www.eol.ucar.edu/rtf/facilities/iss) and by Parsons et al. (1994). The ISS was located at site northwest (NW) on the Colorado Plateau 5 km north-northwest of the crater (Figs. 3a and 3b), where the electronic equipment was housed in a 9-m sea container. The ISS components included a radar wind profiler (RWP) and radio acoustic sounding system (RASS) to make vertical profiles of horizontal wind and virtual temperature through depths of 1–4 and 0.6–1 km above ground level (AGL), respectively, as well as an enhanced automatic weather station that measured wind direction and speed, pressure, temperature, humidity, net radiation, global radiation, incoming longwave radiation, and precipitation. During IOPs, rawinsondes were launched at this site at 3-hourly intervals and tracked using the global positioning system (GPS) to obtain vertical profiles of pressure, temperature, humidity, wind speed, and wind direction to heights of about 20–25 km.

The ISS was supplemented with a minisodar and a second RASS to obtain continuous high-resolution, low-level (100–300 m AGL) wind and temperature profiles. The minisodar and RASS were installed at site SW, 2.5 km southwest of the crater center (Fig. 3b) to eliminate radio interference between the RASS at the minisodar site and the RASS at the RWP site. Collocated at SW was an Integrated Surface Flux Facility (ISFF) micrometeorological tower that was designed to allow comparisons to be made between the surface energy budgets inside and outside the crater.

Data from the ISS sites are being used to test hypotheses concerning the susceptibility of the crater cold pool to larger-scale flows above and upwind of the crater. Additionally, the rawinsonde ascents (temperature and humidity profiles) are being used with tethered soundings inside the crater for radiative transfer computations.

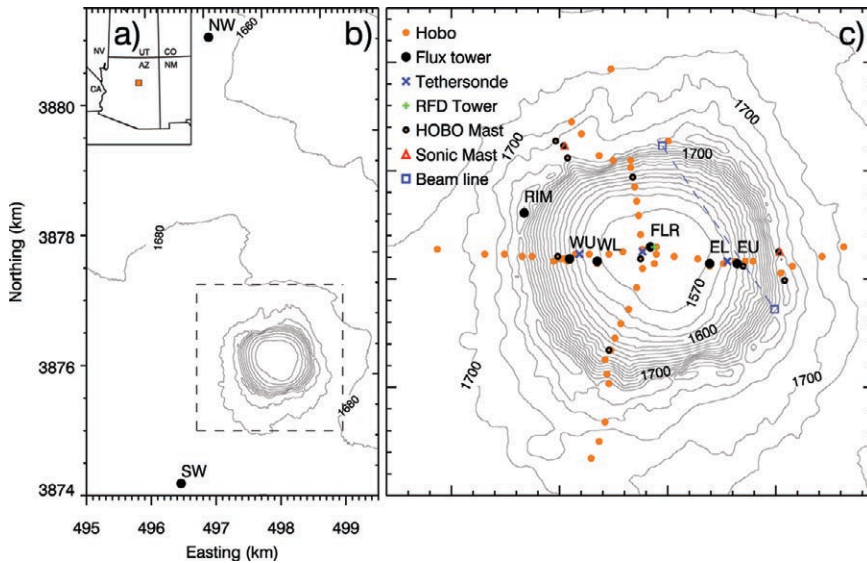


FIG. 3. Instrument locations. (a) Location of Meteor Crater in Arizona. (b) NW was instrumented with a rawinsonde set, a radar wind profiler, a radio acoustic sounding system, an automatic weather station, and radiometers; SW was instrumented with a minisodar, a radio acoustic sounding system, an ISFF tower and a HOBO. (c) Instruments located in or immediately around the crater are detailed in the legend. (b) has a 20-m contour interval, while (c) has a 10-m interval. RFD in the legend stands for radiative flux divergence.

Meteorology inside the crater. The measurement sites inside the crater are shown on the topographic map of Fig. 3c. The measurement equipment is described below.

ISFF MEASUREMENTS. The main continuously operated research instrumentation inside the crater were seven ISFF towers supplied by NCAR to measure turbulent fluxes of momentum, sensible heat, and latent heat by eddy correlation; temperature and humidity profiles; three-dimensional mean and turbulent wind profiles; soil parameters including soil temperature, moisture, heat flux, and soil thermal properties; and long- and shortwave radiative fluxes. ISFF equipment, sensor characteristics, and data processing procedures are described online (www.eol.ucar.edu/rtf/facilities/isff).

Meteorological instruments at the ISFF sites were installed on guyed 6- and 10-m towers. Six-meter towers were installed on the upper east and west sidewalls. Ten-meter towers were installed at the crater floor, and on the lower east and west sidewalls, on the west rim of the crater at Barringer Point (1,744 m), and at site SW outside the crater. The sensor configurations for the towers and tripods are indicated schematically in Fig. 4. The radiation and surface/subsurface measurements at each of the towers were made

from a sawhorse-shaped instrument mounting unit located approximately 15–20 m from the foot of each tower.

Meteorological sensors at each tower were connected to a local data acquisition system taking samples of the meteorological variables at set sampling intervals and making on-site calculations of first and second moments of the high-sample-rate data. Sampling intervals were 1 Hz for most instruments, 20 Hz for sonic anemometers and Krypton hygrometers, and 0.2 Hz for radiation and soil sensors. Five-minute-average data were sent out of the crater from each of the sites through a radio frequency link and repeater to the

ISFF base trailer located outside the crater about 1.5 km south-southwest of the crater center. The performance of the instruments could thus be monitored remotely, with two-way communications between the tower data acquisition systems and the ISFF base. The data throughput of the communications system proved insufficient to bring all the high-rate data (e.g., from the 22 sonic anemometers) out of the crater. Therefore only critical data were sent through the communications system. The full dataset from each tower, however, was stored on 60-GB hard drives that were downloaded manually at about weekly intervals.

The ISFFs were deployed to detect seiches through high-frequency sampling of wind, temperature, and pressure at multiple levels on the towers and to measure slope flow characteristics and surface radiation and energy budget components to test hypotheses concerning the roles of turbulent sensible heat fluxes, radiative fluxes, and slope flows on the buildup and breakdown of the stable boundary layer (SBL). The *crater rim* ISFF measured the strength and characteristics of the flows approaching the crater and the radiative fluxes at the elevation of the crater rim. The *crater floor* ISFF measured the surface radiation and heat fluxes and the evolving characteristics of the nighttime SBL and daytime convective bound-

ary layer (CBL) over the basin center. The daytime CBL was expected to grow rather quickly beyond the depth of the ISFF tower, but the CBL's full depth and characteristics were tracked by tether sondes. The *sidewall* ISFF towers measured the evolving radiative and heat fluxes that drive the slope flows, as well as the time-varying characteristics of both the up- and downslope flows.

Because of asymmetric heating of the crater walls by the sun, especially near sunrise and sunset, strong differences in the surface radiation and energy budgets were expected between the west and east sidewalls. The heating asymmetries were expected to produce interesting asymmetries in boundary layer structure during inversion buildup and breakup that could be observed with direct measurements of CBL depths and upslope and downslope flow characteristics on the different slopes. To test these concepts further, we made extensive observations of ground heat flux, radiative fluxes, surface radiative temperatures, and convective fluxes on the east and west sidewalls and floor of Meteor Crater. The radiation measurements included observations of both slope-parallel and horizontal radiative fluxes. Several redundant measurements were taken (downward-looking pyrgeometers and IR-radiating temperature sensors; net radiation measurements with net radiometers and summed broadband components from upward- and downward-looking pyrgeometers and upward- and downward-looking pyranometers) to evaluate instrument accuracy. Solar diffuse radiation was measured at the crater rim and on the crater floor. Latent heat flux was measured to determine the impact of dewfall and evaporation on the surface heat budgets and on the heat budget of the stable air

mass enclosed within the crater (Whiteman et al. 2007). Measurements of longwave radiative fluxes and surface radiating temperatures were made to support 3D radiative transfer modeling within the crater atmosphere. To further support such modeling, deep temperature and moisture profiles through the crater, the troposphere and upper atmosphere are being composited from the tower profiles, the tether sonde soundings, the ISS rawinsonde soundings, and climatological soundings of the upper atmosphere from the National Weather Service (NWS) radiosondes at Flagstaff.

TETHERED BALLOON SOUNDING SYSTEMS. The evolution of the crater atmosphere and asymmetries in the internal cold pool temperature and wind structure were measured with three tether sondes that were flown concurrently from locations

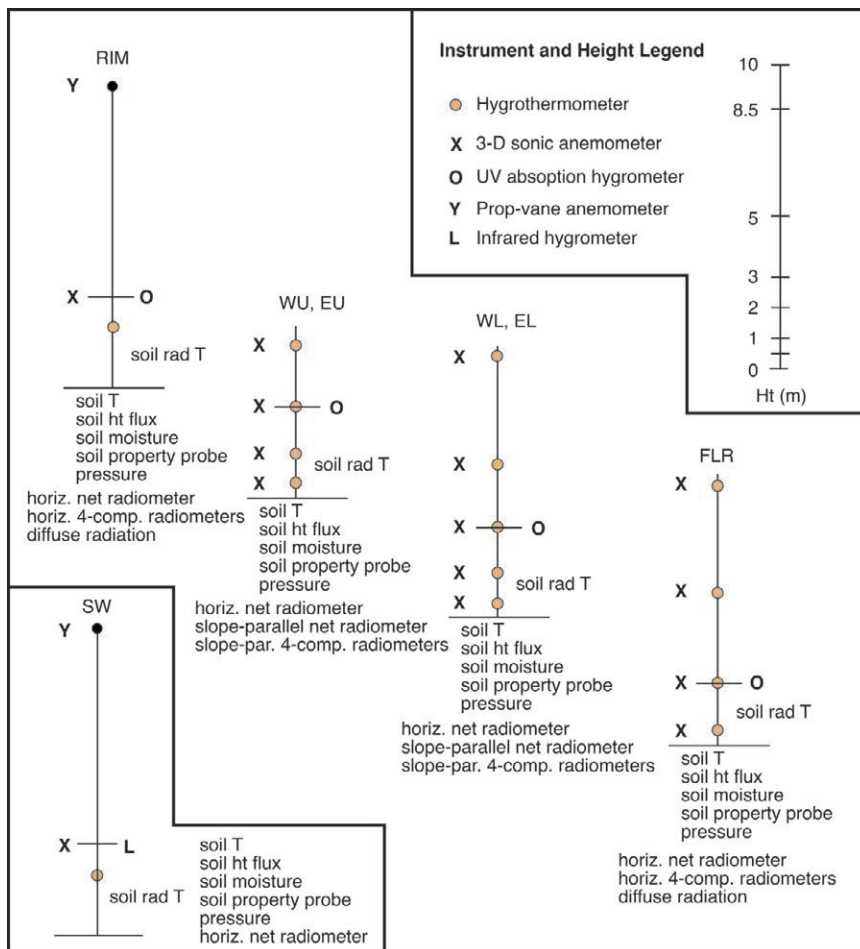


FIG. 4. Instrumentation on the ISFF towers and tripods. The EU and EL towers were instrumented like the WU and WL towers except that Vaisala 50Y hygrothermometers in radiation shields replaced the aspirated NCAR TRH hygrothermometers at all levels except the first level of EL.

on the lower east and west sidewalls and at the crater floor center (Fig. 3c). A Vaisala Digicora Tethersonde System was used for this purpose. The ground-based portion of this sounding system was housed in a tent at the center of the crater floor. Portable gasoline-powered generators at the three tethersonde flight locations provided power for an electric winch that was attached by a line to a 3-m³ blimp-shaped, helium-filled balloon. A battery-powered, meteorological sonde was attached to each tether line approximately 3 m below the balloon, and ascents and descents were made under operator control. The soundings were coordinated by a receiver operator at the tent so that the sondes ascended and descended in unison and were concurrently at approximately the same altitude. Data from the three sondes were transmitted to the ground station receiver. A field comparison of data from the three sondes and a recalibration of the wind direction unit were made at each battery change (typically after every three to five ascents). On reaching the apex of the slow ascents the balloons were retrieved quickly and allowed to equilibrate at the ground before the next ascent.

The tethersonde system was originally designed by the manufacturer for use in a “tower” mode in which multiple sondes were left in place on the tetherline of a single balloon that is tethered at a fixed height. The “profiling” mode of operation that we used, in which the balloon ascends/descends continuously, required some modifications to equipment and procedures to reduce the degradation of wind speed data in this mode. The wind is sensed from a vane, which is free to pivot about the tetherline to point into the wind. The tail of the vane has horizontal and vertical fins. The presence of the horizontal fin causes the vane to assume an upward angle of attack when the balloon is ascending, with the angle of attack increasing with the speed of ascent. The nonhorizontal angle of attack erroneously reduces the horizontal wind speed. We initially removed the horizontal fin and used a harness of our own design that kept the wind vane horizontal. This harness, however, did not handle well in turbulence. We thus resorted to starting the ascent with the center of gravity of the vane forward of the tetherline so that the anticipated constant speed of ascent would cause the vane to tilt into a horizontal attitude. While this worked reasonably well, the limitations of the manufacturer’s design for this mode of operation should be kept in mind when interpreting the data.

The frequency of tethersonde soundings varied depending on the rate of change of cold pool structure (e.g., higher-frequency soundings during the morning

and evening transition periods) and when seiches were indicated by the real-time data. The shortest interval between adjacent sounding start times was about 15 min, although 30 min was more typical. Soundings began around 1600 mountain standard time (MST) and were continued all night and through the next morning until the inversion broke at around 0900 MST. Soundings were made to approximately 100 m above the crater rim but were occasionally extended at the central site to 250 m above the crater rim to detect and record any temporal changes in the background conditions above the crater. Four hundred thirty-one separate soundings were obtained during the seven IOPs.

TEMPERATURE DATALOGGERS. Two lines (north–south and east–west) of temperature dataloggers intersected at the center of the crater floor (Fig. 3c) and extended well outside the crater so that temperatures inside and outside the crater could be compared. The HOBO Pro Temp/Ext Temp temperature data loggers (Onset Computer, Inc., Bourne, Massachusetts) were attached to the undersides of the mounting brackets of six-plate solar radiation shields and installed at 1.2 m AGL on steel fence posts. Air temperature measurements were made at 5-min intervals between 11 July and 31 October 2006. Previous experiments (Whiteman et al. 2000) with the epoxy-potted thermistor temperature sensors found that time constants are about 120 s. Loggers inside the crater were expected to document any microclimatic differences between crater exposures and to determine whether pseudovertical profiles from the lines of HOBOS are useful proxies for free air temperature profiles over the basin center as measured by the tethersondes.

Ten-minute observations were taken from September 2005 into early November 2006 by two HOBOS, one installed on the crater floor and another installed on the north rim, to determine the seasonal dependence of temperature inversions in the crater over a complete annual cycle.

RADIATION FLUX DIVERGENCE TOWER. A 9-m tower was installed on the crater floor (Fig. 3c) next to the central ISFF tower to make direct measurements of longwave radiative flux divergence. Such measurements require a careful relative calibration of the pyrgeometers. Only few such measurements had been made previously (see Sun et al. 2003; Hoch et al. 2007). To observe the radiative heating and cooling rates within three layers, eight pyrgeometers (Kipp and Zonen CG4

were installed in upward- and downward-looking pairs at heights of 0.5, 2, 5, and 8.9 m AGL. These observations are being compared to three-dimensional radiative transfer calculations to investigate the role of radiative flux divergence on cold-air pool evolution. Observations of sensible heat flux at the same heights on the adjacent ISFF tower will be used to test the relationship between sensible and radiative heat flux divergences in the near-surface atmosphere. The observations of temperature tendency (total heating rate) at the ISFF tower are supported by additional measurements of the temperature profile using low-mass thermocouples in the 0–2-m AGL layer in very high vertical resolution at the base of the tower.

SONIC AND HOBO MASTS AND SCINTILLATION MEASUREMENTS FOR SEICHE DETECTION. Measurements aimed at quantifying seiche and internal wave dynamics during the METCRAX field program were guided, in part, by numerical simulations performed for an idealized (azimuthally symmetric) Meteor Crater in advance of the field measurements. These simulations employed a spectral element (SE) code that describes general flows with a series of 3D spectral elements that may have arbitrary shape, with the flow within each element described by a truncated series of Legendre polynomials. For initial simulations, the model resolution was concentrated within Meteor Crater and we imposed inflow–outflow conditions, a no-slip surface condition, and both mean and oscillatory boundary layer flows over the crater. The boundary layer flows excited a 3D internal wave field in the boundary layer above the crater rim, and seiches within the crater. The most interesting dynamical response was sloshing motions within the crater boundary layer accompanying the seiches that led to a spill-out of boundary layer air over the crater rim. Because of these simulations, additional METCRAX instrumentation was placed at the crater rim.

In response to the model simulations, a third mode of operation was used for seiche and internal wave measurements, focused mainly on the crater rim. There, two types of portable masts were instrumented with either multiple HOBOS or multiple sonic anemometers to obtain high-rate wind and temperature profile data (Fig. 3c). Additionally, a Schmidt–Cassegrain telescope for measuring turbulence- and wave-induced optical amplitude fluctuations (scintillation) and angle-of-arrival fluctuations (image motion) was deployed at a site inside the crater, with a 900-m line-of-site path to an array

of Krypton-bulb light sources on the southeast rim of the crater.

The two sonic masts were installed at saddle points on the east and northwest rims. Sonic anemometers were placed at heights of 1.5-, 2.5-, and 6-m levels on each of the two 6.4-m masts. A fourth sonic anemometer was placed on the northwest rim at 0.5-m AGL height. Dataloggers (Behn et al. 2008) continuously recorded and time-stamped sonic data collected at the two sites, utilizing GPS timing to correct for drift in the local personal computer clock.

Six lightweight HOBO masts, with HOBOS at the 0.5-, 1.0-, 1.5-, 2.0-, and 2.5-m AGL levels of the 3-m masts, were deployed at various places and times on the crater rim and inner sidewalls. Temperature data on these masts were sampled at 0.2 Hz. During the first week of operation, two of the HOBO masts were operated near the northwest sonic tower to gather supplementary data. A HOBO mast was also installed on the east rim. In the last week of the deployment four of the HOBO masts were installed north, east, south, and west of the crater center on the middle to upper sidewalls to gain additional information at these undersampled altitudes.

Scintillation and image motion measurements from the telescope were made on three evenings. Seiche activity was expected to occur mostly in the east–west direction because of the prevailing westerly and southwesterly background flows, so the optical propagation path was chosen on a north–south axis on the east side of the crater. The telescope was focused on the bulb array, and the resulting images were captured with a charge-coupled device (CCD) camera at about 30 frames per second. Offline image processing provides vertical and horizontal centroid coordinates for each of the four point sources. The frequency spectra and cross-spectra of the centroids are being analyzed to retrieve information about turbulence, winds, and waves. The theory and application of this technique were described by Cheon and Muschinski (2007) and Cheon et al. (2007).

OBSERVATIONS AND PRELIMINARY ANALYSES. *Synoptic meteorology.* October 2006 began with an upper-level longwave ridge centered over the central United States. By 4 October an upper-level cutoff low formed in the southwestern United States. This persisted through 15 October, bringing generally variable and unsettled weather. The position of the low brought stronger southwesterly flows and a moisture flux from the tropics. The low was ejected from the southwestern United States during the middle of the month by a kicker trough bringing

high pressure to the region for 21–24 October. The remainder of the month was characterized by a progressive pattern with two fast-moving shortwave troughs that moved through Arizona by 31 October.

The National Centers for Environmental Prediction (NCEP) North American Regional Reanalysis (NARR; Mesinger et al. 2006) shows lower-than-average 500-hPa heights to the west of the study region in October, with a center just off the coast of California. This caused October 700-hPa meridional winds to be 1–2 m s⁻¹ above average in northern Arizona, but with near-average zonal winds. The anomalous cutoff low also brought above-average October precipitation to northern Arizona.

Forecasting for IOPs was accomplished with assistance from the NWS Forecast Office in Flagstaff. IOPs were scheduled on nights when we expected quiescent conditions (clear skies and near-calm surface winds) and maximum cold pool formation in the crater. IOP forecast criteria included upper-level high pressure over the western United States, weak upper-level and midlevel mesoscale wind speeds, weak low local surface wind speeds in the Meteor Crater region, low moisture availability at all levels, and clear skies.

Despite successful forecasts of quiescent background synoptic conditions, tethersonde operations during several IOPs were interrupted by unexpected turbulence episodes at night, especially at the tethersonde site on the west sidewall. The wind measurements made outside the crater revealed that shortly after sunset on synoptically undisturbed nights, low-level winds regularly turned to blow from southwest. This directional shift was very often accompanied

by an increase in wind speed from 1–2 m s⁻¹ in late afternoon to more than 5 m s⁻¹. Figure 5 shows daytime and nighttime wind roses using the 10-m, 5-min-average wind data at the NW site for the entire month. The daytime winds exhibited a wide distribution in direction, while the nighttime winds were predominantly from the southwest. The distribution of wind speeds is also quite different, with daytime speeds varying over a wide range while nighttime winds showed a single peak between 4 and 6 m s⁻¹. Further examination linked this nocturnal southwesterly wind to a regional-scale downslope flow that develops at night over the rising ground to the southwest of the crater, which culminates in the Mogollon Rim. The detailed structure and evolution of this regional-scale downslope flow and its interaction with synoptic conditions are described by Savage et al. (2008).

Seasonal distribution of inversions in the crater. The long-term availability of HOBO temperature data from sites on the crater rim and floor allowed a seasonal analysis of the strength and duration of temperature inversions in the crater. The maximum and minimum daily temperature differences between the rim and floor of the crater are plotted in Fig. 6. From this we see that temperature inversions are strongest in midwinter, when rim-floor temperature differences can exceed 15°C in the 165-m-deep crater. The minimum temperature differences also show that lapse conditions form daily in the crater, with no events in the period of record when the nighttime inversion persisted throughout the day.

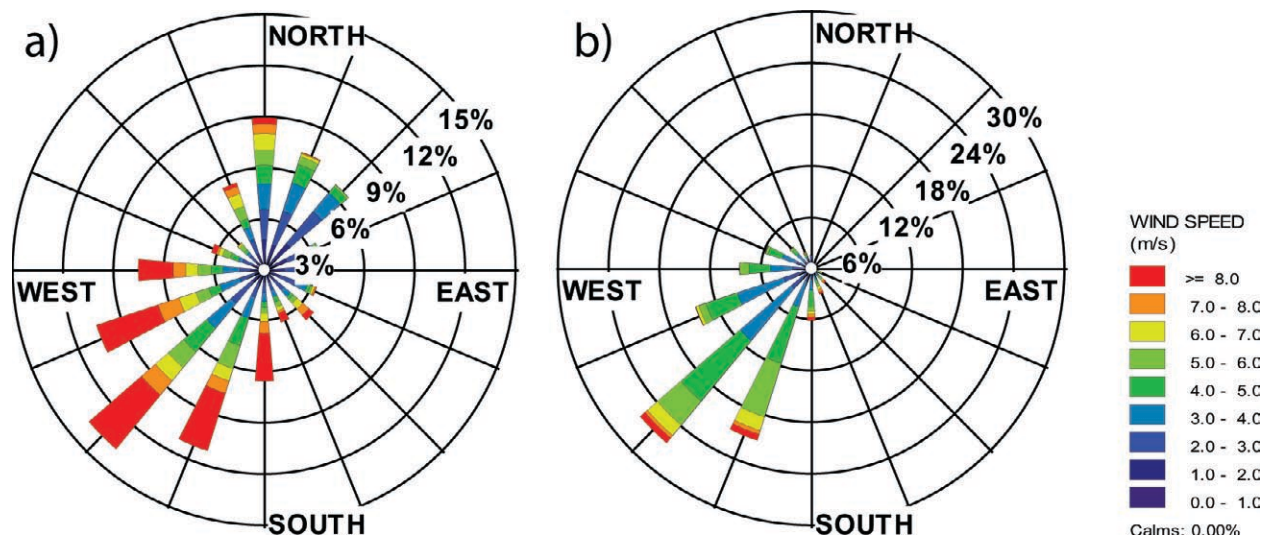


FIG. 5. (a) Daytime (0600–1800 MST) and (b) nighttime (1800–0600 MST) wind roses for the period from 27 Sep through 1 Nov 2006, NW site.

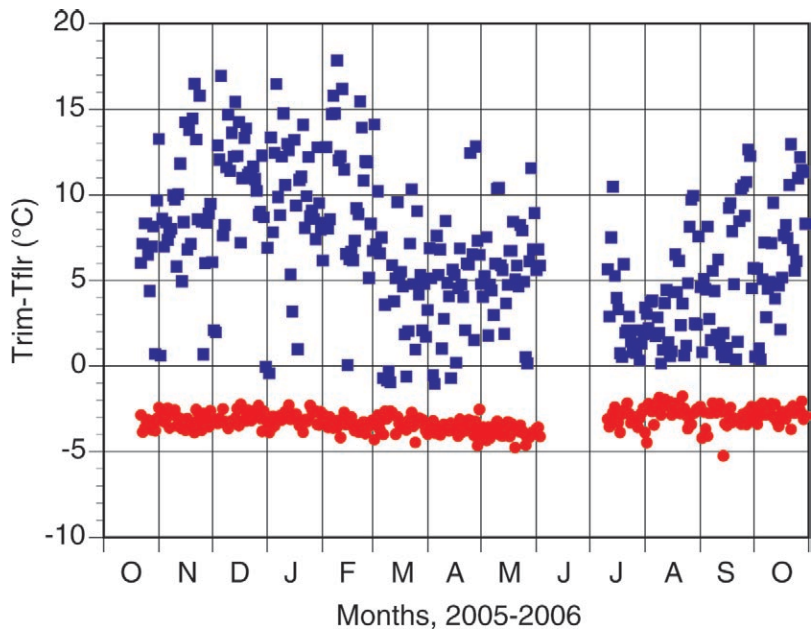


FIG. 6. Daily maximum (blue) and minimum (red) values of the temperature difference between the rim and floor of the crater as a function of day of year.

Sidewall temperature evolution and temperature oscillations. The HOBO temperature datalogger lines on the north, east, south, and west sidewalls of the crater support a variety of meteorological analyses. Here, we present two analyses. In the first (Fig. 7), time series of 5-min temperature observations for the clear 24-h period starting at noon on 22 October are shown for the portion of the west sidewall line inside the crater. The west sidewall line started at the valley floor center (site C00) and ran up the west sidewall to the crater rim (sites W01 through W09). The key feature of the data is the strong nighttime cooling at the lowest elevation sites and the consequent formation of a strong but shallow temperature inversion between sites C00 at 1,564 m and W04 at 1,591 m. At elevations above site W04 the crater sidewall is approximately isothermal. At midday the higher-altitude sites have lower temperatures because temperatures decrease with altitude in the

well-mixed atmosphere. Sharp temperature decreases at the individual sites in the afternoon (and sharp temperature jumps in the morning) clearly indicate the times of local sunset and sunrise at the individual sites as shadows propagate across the crater. Especially prevalent during this night are oscillations in temperature at the lowest-altitude sites and a disturbance that produces vertical mixing and warming at the low-altitude sites around midnight.

When winds above the crater exceed 5 or 6 m s⁻¹, it is difficult for a temperature inversion to form in the crater. Figure 8 illustrates this for the night of 30–31 October, when strong winds above the crater oscillated in speed. Decreases in winds allowed the temperature inversion

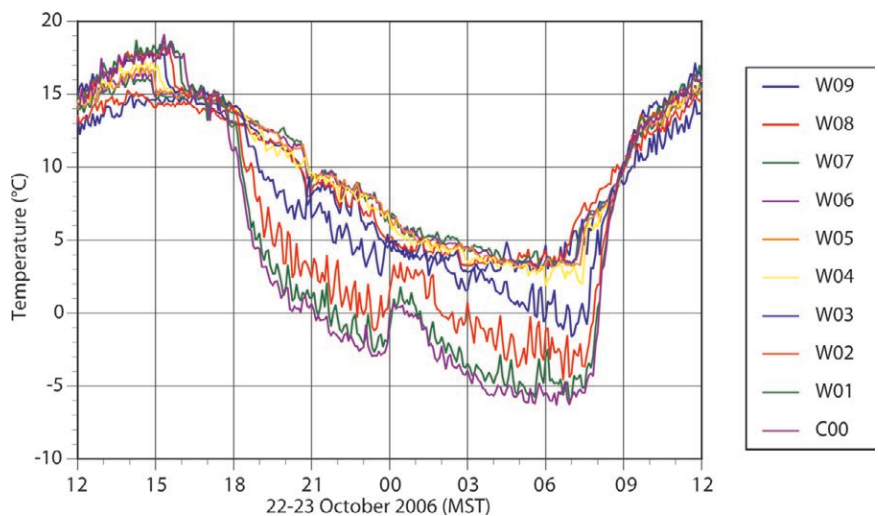


FIG. 7. Temperature time series for HOBO sites on the west sidewall on 22–23 Oct, illustrating the temperature oscillations caused by internal wave motions.

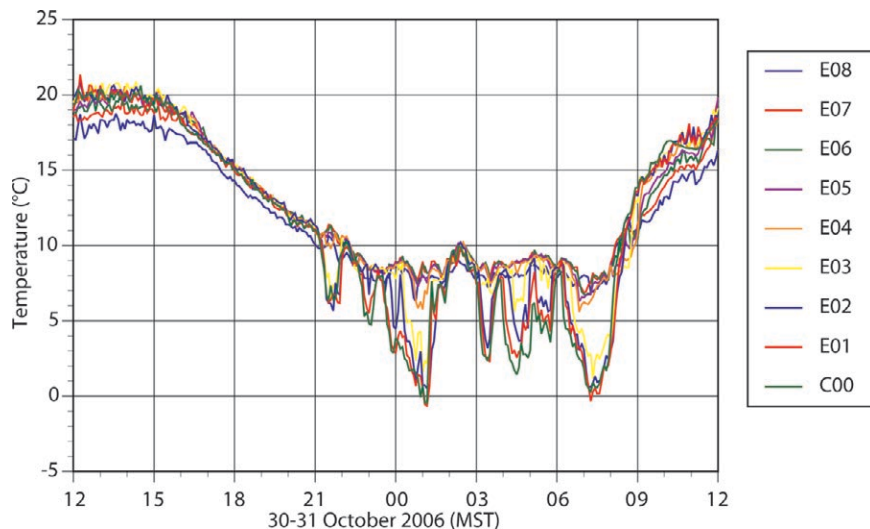


FIG. 8. Temperature time series for HOBO sites on the east sidewall on 30–31 Oct, illustrating the occasional break in of winds that destroy the incipient crater temperature inversion.

Seiches. One of the main goals of METCRAX was to investigate the structure and evolution of standing internal waves or seiches in the crater cold-air pool. Figure 9 shows two time series of the zonal wind velocity during the period from 0100 to 0700 MST on 23 October 2006. The data shown are 1-min averages measured at the bottom of the crater at 2.0 and 8.5 m AGL. As expected, the wind velocity oscillates with time. The mean value at both heights was close to zero and typical values of the amplitudes are between 0.5 and 1.0 m s^{-1} . Most of the time, the velocity perturbations at the two heights are in phase and have nearly the same amplitude. During the period between 0200 and 0400 MST, however, the amplitude at 8.5 m is much smaller than that at 2.0 m, indicating that the seiches occurred only in a very shallow layer (less than 8.5-m thickness) during this time, while the “sloshing layer” was thicker than 8.5 m during the rest of the observed period. The dominating seiche period was about 15 min.

Inversion structure and evolution. Selected ascents from the tethersonde at the crater floor center illustrate the evolution of temperature structure in and above the crater during the evening transition period on the clear, low-winds aloft night of 22–23 October.

The evening temperature structure evolution is illustrated in Fig. 10. The 1600 MST sounding showed a shallow superadiabatic layer at the crater floor surmounted by a near-neutral layer that extended through the depth of the crater and into the atmosphere above. Astronomical sunset was at 1738 MST, but local sunset at the central tethersonde site was at 1606 MST. A 25-m-deep temperature inversion formed over the crater floor by 1730 MST and, by 1830 MST, grew to a depth of 50 m with an especially strong cooling near the crater floor. A

near-isothermal layer formed above the inversion. During the remainder of the evening, the air within the crater continued to cool but maintained the same basic temperature structure—a shallow surface-based inversion surmounted by a near-isothermal layer. Because of the more rapid cooling inside the crater compared to that of the atmosphere above the crater, a temperature jump developed at the level of the crater rim. The development of a deep near-isothermal layer in the upper 80% of the crater atmosphere is a surprising result that differs from nighttime profiles observed in other similar-sized basins (Clements et al. 2003; Steinacker et al. 2007). A number of hypotheses, including mixing, radiative transfer, and air incur-

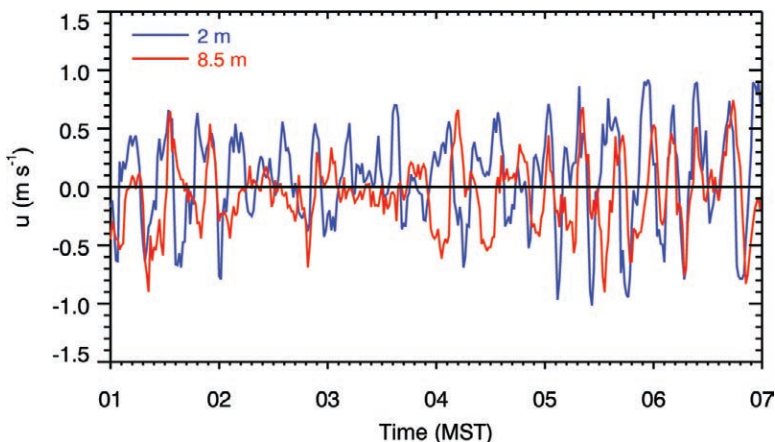


FIG. 9. One-minute-average zonal wind velocity at the 2- and 8.5-m levels on the crater floor (FLR) on 23 Oct.

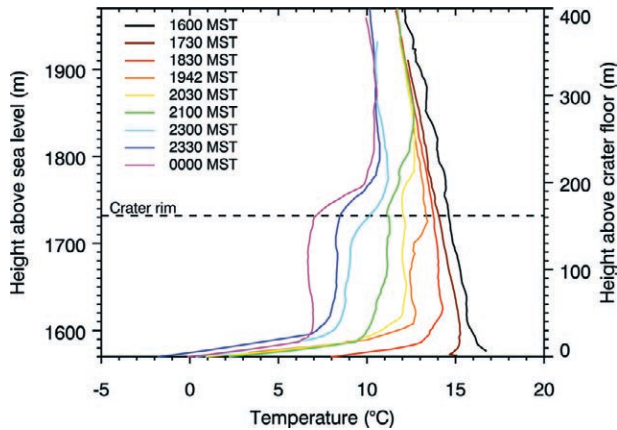
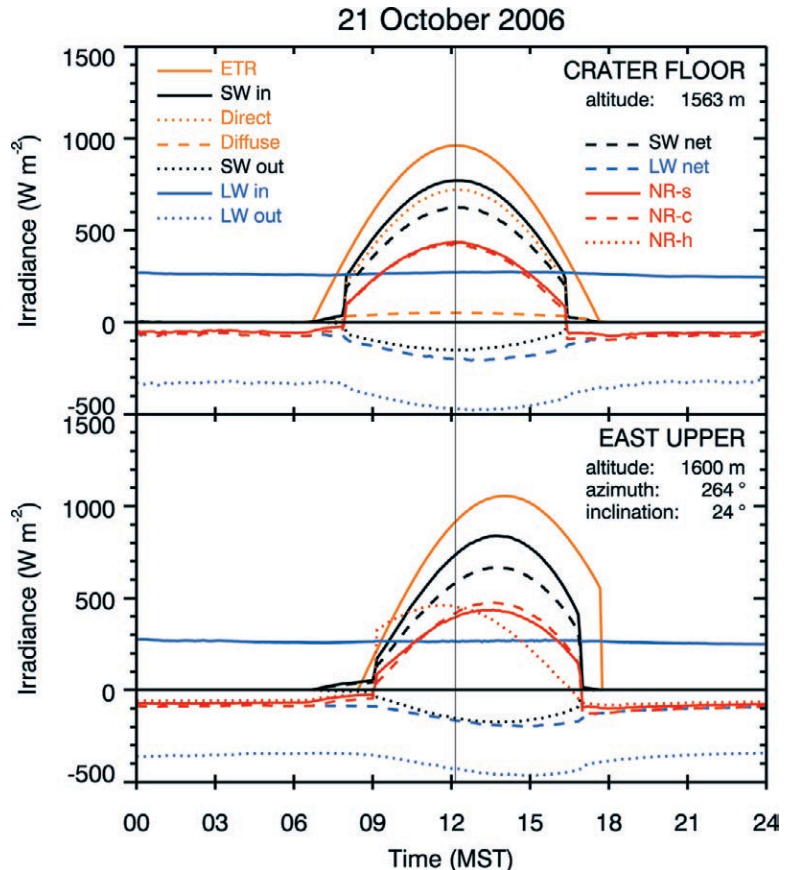


FIG. 10. Selected tethersonde soundings from the center of the crater floor illustrating temperature profile evolution during the evening of 22 Oct. Sounding times are given in the legend.

sions across the rim, are presently being evaluated to explain these observations.

Surface radiation and energy budgets. Individual components of the surface radiation and energy budgets were measured at the six ISFF tower sites in the crater and on the rim. The incoming and outgoing short- and longwave radiation components as well as net radiation were measured parallel to the underlying slope. Diffuse radiation was measured at the crater floor and rim sites, where the underlying surface was horizontal. At the sites

FIG. 11. Radiative fluxes at the crater floor site (top) and the upper east sidewall site (bottom) on the clear day of 21 Oct. The vertical gray line marks the time of solar noon. Individual radiation budget components include the calculated extraterrestrial flux (ETR); the directly measured global (SW in), diffuse, shortwave reflected (SW out), longwave incoming (LW in), longwave outgoing (LW out), net radiation (NR-s), and horizontal net radiation (NR-h) fluxes. Variables calculated from these quantities and shown in the figure are net radiation (NR-c, sum of the four components SW in, SW out, LW in, and LW out), direct radiation (global minus diffuse), shortwave net radiation (SW net), and longwave net radiation (LW net).



on the crater sidewalls, additional net radiometers were mounted horizontally.

Five-minute averages of the surface radiation budget components for the crater floor and upper east sidewall sites on a clear day are shown as an example in Fig. 11. On 21 October, astronomical sunrise was at 0639 MST and astronomical sunset was at 1740 MST. The maximum global solar radiation was attained shortly after solar noon (indicated by a vertical line in Fig. 11). The shading of the sites by the crater sidewalls delayed sunrise at both the crater floor (0800 MST) and upper east sidewall (0903 MST), and led to an earlier sunset (crater floor: 1620 MST, upper east: 1658 MST).

At this arid site, global radiation reaches 80% of the extraterrestrial radiation, net radiation exceeds 400 W m^{-2} , and reflected radiation reaches 19% of global radiation. While the maximum insolation occurs at solar noon at the crater floor, the exposure (slope and azimuth) at the east upper site delays the insolation maximum until 1400 MST.

Because the surface energy budget is driven primarily by net radiation, the significant differences between the measured net radiation on horizontal and sloping surfaces at this arid site suggest that

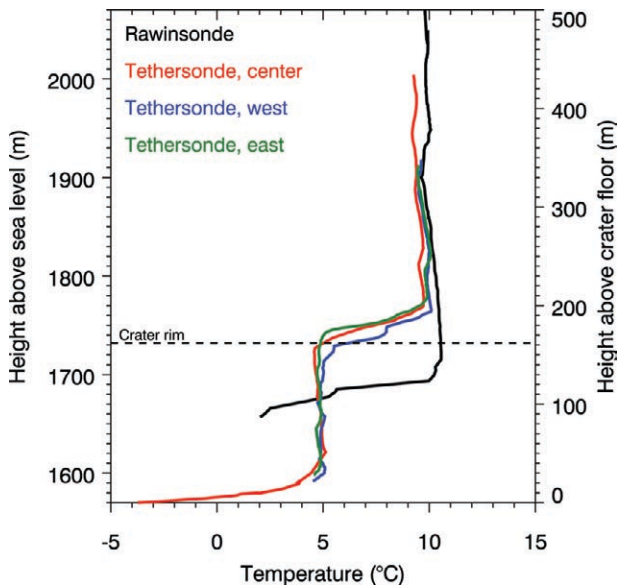


FIG. 12. Coincident temperature soundings made from the east (green), central (red), and west (blue) tether sondes inside the crater and the rawinsonde (black) outside the crater at 0308 MST 23 Oct.

significant sensible heat flux differences will be seen between the crater floor and sidewall sites—a subject for further analysis.

Crater-plain temperature structure differences. Some interesting differences were found between the temperature structure inside the crater, as determined from the three tether sonde sites, and the temperature structure outside the crater, as determined from rawinsondes. Figure 12 compares four temperature soundings taken at 0300 MST 23 October 2006. The three tether sonde soundings inside the crater, despite their widely separated locations at the crater floor center and on the lower east and west sidewalls, indicated nearly identical temperature structures inside the crater. The atmosphere inside the crater was, thus, approximately horizontally homogeneous. The temperature jump at the top of the isothermal layer, however, was found at a lower altitude near the rim level over the west sidewall than over the crater center or eastern sidewall. A mesoscale drainage wind from the southwest was often present on IOP nights and its descent in the lee of the crater rim is thought to be responsible for depressing the top of the temperature jump on the west side of the crater, a feature that is seen more prominently on other nights. The rawinsonde sounding outside the crater (black line in Fig. 12) can be compared to the tether sonde soundings. The crater atmosphere is significantly colder than the atmosphere surrounding the crater,

except for a shallow layer at 2/3 the depth of the crater, a height corresponding to the altitude of the surrounding plain at the NW site, which is covered by a shallow but strong inversion.

There were a number of instances when cold-air pools that developed in the crater were later disturbed by strong southwesterly background winds that arose during the night. Surprisingly, these winds would mix warmer air from aloft downward over the crater slopes, while leaving the inversion intact over the crater center.

SUMMARY AND OUTLOOK. A meteorological field campaign was conducted during the month of October 2006 in Arizona's Meteor Crater to study the development of the stable boundary layer and to determine the existence and characteristics of atmospheric seiches in the crater. With NCAR support, data were collected continuously at multiple locations in and around the crater. In addition, observations were taken in clear, light wind conditions during seven IOPs. The resulting extensive datasets are now being analyzed, and numerical model simulations are being performed.

Observations show that nighttime temperature inversions form frequently in the crater, and that the crater atmosphere structure evolves differently from other basins that have been previously studied. Internal wave motions are common in the crater SBL and a seiche episode has been documented on the crater floor. The diurnal propagation of shadows and solar radiation produce important effects on the surface radiation budget. This should translate into significant nonstationary spatial gradients in the surface energy budget, with implications for the development and phasing of slope flows. The crater atmosphere has been shown to be subject to the influence of mesoscale drainage flows coming from the higher elevations southwest of the crater. Further studies of the roles of slope flows, turbulence, radiative flux divergence, internal wave motions, seiches, and background winds on the development and evolution of the SBL in the crater are underway and will be published as they are completed. The dataset should prove especially valuable for the verification of numerical models, and we plan, for example, to extend the SE model to investigate radiatively driven slope flows within the crater. It is hoped that an improved basic understanding of the SBL evolution and dynamics from the rather idealized topography of Meteor Crater will lead to future practical improvements in air pollution forecasting and management, local weather forecasting, ground transportation

management, emergency response management, and land-use planning in complex terrain. Meteorological data from METCRAX 2006 are now available through the NCAR ISS and ISFF Web sites and through links from these sites to those of the METCRAX principal investigators.

ACKNOWLEDGMENTS. NCAR's Earth Observing Laboratory provided equipment, field support, and data processing services. Barringer Crater Corporation (Drew Barringer, President), and Meteor Crater Enterprises, Inc. (Brad Andes, President) provided crater access, and they and their staffs provided outstanding cooperation and assistance. Brian Klimowski and his staff at the NWS Flagstaff Weather Forecast Office provided forecast assistance. Dr. Eric Pardyjak at the University of Utah loaned us a tethered sonde system. Dr. John Wyngaard at The Penn State University loaned us several sonic anemometers, and ETH Zürich loaned us four CG-4 pyrgeometers. We thank METCRAX participants for their field and data processing assistance, including A. J. Ideris, J. Bobka, P. Bogenschutz, T. Brimeyer, E. Crosman, B. Folsom, L. Fusina, C. Golubieski, G. Granger, J. Guard, L. Jones, K. Knudson, S. Krueger, T. Lim, G. Maclean, C. Martin, J. Miltzer, C. Savage, N. Schiffer, S. Semmer, J. Thibodeaux, T. Thompson, L. Tudor, L. Verstraete, M. Verstraete, C. Wall, J. Whiteman, J. Wofsy, F. Wrenn, and K. Young. We thank three anonymous reviewers for their constructive suggestions on the manuscript.

This research was supported by NSF's Physical and Dynamic Meteorology Division (S. Nelson, Program Manager) through Grants ATM-0444688 (Muschinski), 0444441 (Fritts), 0444807 and 0646206 (Zhong), and 0444205 and 0521776 (Whiteman) and in part by the U.S. Army Research Laboratory and the U.S. Army Research Office under Grants 49393-EV (Muschinski) and 52734-EV (Whiteman and Hoch). S. W. Hoch was supported by an Individual Support Fellowship from the Swiss National Science Foundation.

REFERENCES

- Behn, M., V. Hohreiter, and A. Muschinski, 2008: A scalable data-logging system with serial interfaces and integrated GPS time-stamping. *J. Atmos. Oceanic Technol.*, **25**, 1568–1578.
- Cheon, Y., and A. Muschinski, 2007: Closed-form approximations for the angle-of-arrival variance of plane and spherical waves propagating through homogeneous and isotropic turbulence. *J. Opt. Soc. Amer.*, **24**, 415–422.
- , V. Hohreiter, M. Behn, and A. Muschinski, 2007: Angle-of-arrival anemometry by means of a large-aperture Schmidt-Cassegrain telescope equipped with a CCD camera. *J. Opt. Soc. Amer.*, **24**, 3478–3492.
- Clark, R. H., A. J. Dyer, R. R. Brook, D. G. Reid, and A. J. Troup, 1971: *The Wangara Experiment: Boundary Layer Data*. Commonwealth Scientific and Industrial Research Organization, 316 pp.
- Clements, C. B., C. D. Whiteman, and J. D. Horel, 2003: Cold-air-pool structure and evolution in a mountain basin: Peter Sinks, Utah. *J. Appl. Meteor.*, **42**, 752–768.
- Doran, J. C., and T. W. Horst, 1983: Observations and models of simple nocturnal slope flows. *J. Atmos. Sci.*, **40**, 708–717.
- Grubišić, V., and Coauthors, 2008: The Terrain-Induced Rotor Experiment: An overview of the field campaign and some highlights of special observations. *Bull. Amer. Meteor. Soc.*, **89**, 1513–1533.
- Haugen, D. A., J. C. Kaimal, and E. F. Bradley, 1971: An experimental study of Reynolds stress and heat flux in the atmospheric surface layer. *Quart. J. Roy. Meteor. Soc.*, **97**, 168–180.
- Hoch, S., P. Calanca, R. Philipona, and A. Ohmura, 2007: Year-round observations of longwave radiative flux divergence in Greenland. *J. Appl. Meteor. Climatol.*, **46**, 1469–1479.
- Horst, T. W., and J. C. Doran, 1986: Nocturnal drainage flow on simple slopes. *Bound.-Layer Meteor.*, **34**, 263–286.
- Mesinger, F., and Coauthors, 2006: North American Regional Reanalysis. *Bull. Amer. Meteor. Soc.*, **87**, 343–360.
- NCAR, cited 2008a: ISS Page for METCRAX. [Available online at www.eol.ucar.edu/rtf/projects/metcrax/iss/]
- , cited 2008b: NCAR Integrated Surface Flux Facility at METCRAX, October 2006. [Available online at www.eol.ucar.edu/rtf/projects/METCRAX/isff/]
- Parsons, D. B., and Coauthors, 1994: The Integrated Sounding System, Description and preliminary observations from Toga-COARE. *Bull. Amer. Meteor. Soc.*, **75**, 553–567.
- Phillips, F. M., M. G. Zreda, S. S. Smith, D. Elmore, P. W. Kubik, R. I. Dorn, and D. J. Roddy, 1991: Age and geomorphic history of Meteor Crater, Arizona, from cosmogenic C1-36 and C-14 in rock varnish. *Geochim. Cosmochim. Acta*, **55**, 2695–2698.
- Poulos, G. S., and Coauthors, 2002: CASES-99: A comprehensive investigation of the stable nocturnal boundary layer. *Bull. Amer. Meteor. Soc.*, **83**, 555–581.
- Savage, L. C., S. Zhong, W. Yao, W. O. J. Brown, and T. W. Horst, 2008: An observational and

- numerical study of a regional-scale downslope flow in Northern Arizona. *J. Geophys. Res.*, **113**, D14114, doi:10.1029/2007JD009623.
- Schiermeier, F. A., T. F. Lavery, D. G. Strimaitis, A. Venkatram, B. R. Green, and B. A. Egan, 1983: EPA model development for stable plume impingement on elevated terrain obstacles. *Air Pollution Modeling and its Application IV*, C. DeWispelaere, Ed., Vol. 7, Plenum Press, 637–647.
- Smith, M. D., and Coauthors, 2004: First exploration science results from the Mars Exploration rovers Mini-TES. *Science*, **306**, 1750–1753.
- , —, N. Spanovich, A. Ghosh, D. Banfield, P. R. Christensen, G. A. Landis, and S. W. Squyers, 2006: One Martian year of atmospheric observations using MER Mini-TES. *J. Geophys. Res.*, **111**, E12S13, doi:10.1029/2006JE002770.
- Steinacker, R., C. D. Whiteman, M. Dorninger, E. Mursch-Radlgruber, K. Baumann, S. Eisenbach, A. M. Holzer, and B. Pospichal, 2007: A sinkhole field experiment in the Eastern Alps. *Bull. Amer. Meteor. Soc.*, **88**, 701–716.
- Sun, J., S. P. Burns, A. C. Delany, S. P. Oncley, T. W. Horst, and D. H. Lenschow, 2003: Heat balance in the nocturnal boundary layer during CASES-99. *J. Appl. Meteor.*, **42**, 1649–1666.
- Whiteman, C. D., T. B. McKee, and J. C. Doran, 1996: Boundary layer evolution within a canyonland basin. Part I. Mass, heat, and moisture budgets from observations. *J. Appl. Meteor.*, **35**, 2145–2161.
- , J. M. Hubbe, and W. J. Shaw, 2000: Evaluation of an inexpensive temperature data logger for meteorological applications. *J. Atmos. Oceanic Technol.*, **17**, 77–81.
- , S. F. J. De Wekker, and T. Haiden, 2007: Effect of dewfall and frostfall on nighttime cooling in a small, closed basin. *J. Appl. Meteor. Climatol.*, **46**, 3–13.
- Wright, S. P., and M. S. Ramsey, 2006: Thermal infrared data analyses of Meteor Crater, Arizona: Implications for Mars spaceborne data from the Thermal Emission Imaging System. *J. Geophys. Res.*, **111**, E02004, doi:10.1029/2005JE002472.
- Yao, W., and S. Zhong, 2008: Nocturnal temperature inversions in a small, enclosed basin and their relationship to ambient atmospheric conditions. *Meteor. Atmos. Phys.*, in press.